Subsurface Feature-based Ground Robot/Vehicle Localization Using a Ground Penetrating Radar

Haifeng Li[1], Jiajun Guo[1], and Dezhen Song[2]

Abstract— Robot localization using subsurface features captured by Ground-Penetrating Radar (GPR) complements and improves robustness over existing common sensor modalities, as subsurface features are less sensitive to weather, season and surface scene changes. Here, we propose a novel subsurface feature-based localization method that uses only GPR measurements with a known subsurface map. An efficient feature descriptor, the dominant energy curve (DEC), is designed to identify different locations in cluttered conditions. Specifically, image processing techniques that involve background segmentation, energy point detection, and energy curve refinement are designed to extract DEC features from a 2D radargram. With DECs features obtained, a metric subsurface feature map is constructed. Finally, we perform robot localization by feature matching under a particle swarm optimization framework. We have implemented our method and tested it with the public CMU-GPR dataset. The results show that our algorithm improves accuracy and robustness with real-time performance for robot localization tasks. Specifically, the mean localization error is 0.50 **m for all cases.**

I. INTRODUCTION

Robot localization in a Global Positioning System (GPS)-denied environment remains a challenging problem in the field of robotics. Most existing methods rely on sensors such as camera, lidar, or automotive radar. These approaches extract features from the signals reflected from objects in the environment to compute the robot location. However, such appearance-based approaches often face severe challenges under season changes, surface scene changes, or inclement weather conditions such as dense fog, rainstorm, heavy snow, or sandstorm.

In contrast, subsurface objects/features are relatively constant and less likely to be affected by the aforementioned conditions. As a primary sensor for the subsurface scan, Ground-Penetrating Radar (GPR) has been widely adopted in archaeology, landmine identification, utility pipe localization, and concrete inspection. Recently, GPR has also been employed in robot localization. However, current approaches perform localization by matching the current raw GPR readings or simple features with the constructed maps by
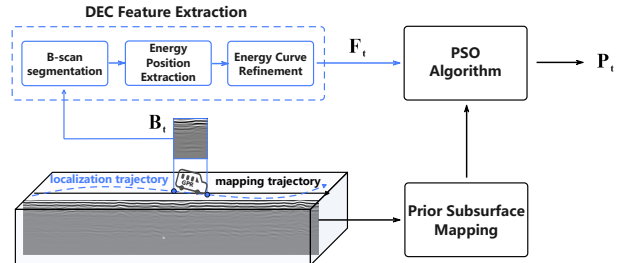
Fig. 1. Illustration of our subsurface feature based localization problem. Blue pipeline is the localization pipeline and black pipeline is the mapping pipeline that builds the prior map for localization.

applying deep learning techniques, leading to problems in reliability and interpretability of subsurface features.

Here we propose a novel feature-based subsurface localization method as illustrated in Fig. 1. An efficient feature descriptor, named as the Dominant Energy Curve (DEC), is designed to identify different locations in cluttered conditions. Using DEC features, we construct the subsurface map and adopt the particle swarm optimization algorithm to estimate the robot position by matching the actual observations and the constructed map. We have implemented our method and tested it on the public CMU-GPR dataset. The results show that our algorithm improves both accuracy and robustness with real-time performance for robot localization tasks. Specifically, the mean localization error is 0.50 m for all cases.

II. RELATED WORKS

The most related works are from GPR in robotic applications, subsurface reconstruction and mapping, and localization and mapping with GPR.

Most GPR usage in robotics is for non-destructive evaluation applications, including bridge deck inspection [1], [2], utility detection [3], [4], airport runway inspection [5], [6], and planetary exploration [7], [8]. In these applications, GPR is used as a sensor to search for and recognize specific subsurface objects or features. Subsurface reconstruction and mapping is another typical GPR application with robots, where the robot is equipped with a GPR to scan an area of interest for the construction of a subsurface map [9]–[11]. However, these works do not attempt to localize robot using the generated map.

Using GPR in robotic localization and mapping has received more attention recently from robotics researchers. Early work in robot localization based on GPR is reported in [12], where a localization GPR (LGPR) module is introduced

as a GPR mounted on a ground vehicle that can localize itself with a prior map. In this method, a grid map consisting of a set of rectangular 3D GPR raw signals with location labels is created in advance and then the current GPR observations are registered in the grid map to find the global position of GPR. This work is further extended to autonomous navigation in variable weather conditions using the same LGPR module [13]. The main issue of the LGPR method is that the raw GPR data are used as features for mapping, and hence the method is sensitive to the varying dielectric properties of the medium during mapping/localization. Therefore, localization and mapping may lack consistence and robustness in long-term applications. Furthermore, the LGPR method needs initial access to GPS signals during operation.

Instead of localizing the GPR on a prior map, Baikovitz et al. propose a GPR-based odometry [14] which models the localization problem as an inference on a factor graph. A key idea of this method is to learn relative sensor models directly from GPR data that map non-sequential GPR image pairs to relative robot motion. They also present an open source GPR dataset, the CMU-GPR dataset [15], for research in subsurface-aided perception for robot navigation, and have tested their method on the CMU-GPR dataset. However, the performance of their proposed method relies on the quality of the learned sensor model, which is sensitive to working conditions and the accuracy of manually labeled training data sets. Furthermore, it is labor intensive and cost prohibitive to obtain representative GPR data for training, especially in real-world applications.

Therefore, extracting stable features from GPR data to perform mapping and localization is a reasonable choice. However, this task is quite challenging, as GPR data often have significant signal clutters. Skartados et al. [16] propose a feature-based GPR self-localization method by isolating spatiotemporal salient regions on consecutive GPR traces. The work assumes a simulated GPR model with subsurface utility pipeline priors. However, neither the GPR model nor the requirement for the presence of subsurface pipelines are easily met in general applications.

Our group has experience in GPR-based robotic inspection and mapping for years. We have adopted GPR in airport runway inspection [5], [6], utility pipeline reconstruction [17] and subsurface mapping [11]. These works lay the foundation for understanding GPR to develop this work where we propose a novel GPR feature descriptor for more efficient subsurface representation and robust robot localization.

III. PROBLEM FORMULATION

A. Working Principles of a GPR

For completeness, let us review the working principles of a GPR [17]. GPR has a transmitter (TX) to transmit radar signals and a receiver (RX) to receive radar signals. Reflection occurs when a radio pulse travels to where dielectric permittivity varies and a reflection of the pulse is received by RX, and according to the traveling time between the emitted radio pulses and the echoed pulses, the processor in GPR generates an A-scan that records the signal amplitude versus
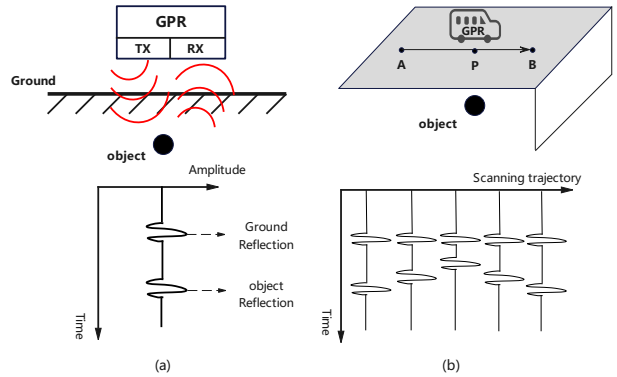

Fig. 2. A simplified visualization of GPR working principle.

traveling time at this GPR position (see Fig. 2(a)). At the top of Fig. 2(b), a GPR travels from point A to B and a ball-shaped object is buried under point p. When the GPR is located at the point p, as shown at the top of Fig. 2(a), a transmitted radio pulse (TX) has two peak reflections, one from the ground reflection and the other from the buried object. The resulting A scan signal is shown at the bottom of Fig. 2(a), the upper peak represents the reflection from the ground and the lower peak represents the reflection from the object. When the GPR travels from A to B, the antenna transmits a series of pulses at different positions, which leads to a series of A-scan signals. A B-scan is defined as the sequence of A-scan signals in chronological order, and a sample B-scan is shown at the bottom of Fig. 2(b). The different reflection peaks position of the object represents different distances of the GPR from the object.

B. Scenarios and Assumptions

Before the localization, we perform an exhaustive pre-scanning process that covers the entire environment to generate a prior map which is illustrated as the black pipeline in Fig. 1. The GPS locations and the corresponding radar feature maps, the format of which will be explained later, are stored in this prior map.

The localization process is to register the current GPR readings with the prior map to find the robot location. To reduce the cost, we employ a single-channel GPR. Since we are interested in re-localization with subsurface information matching, we assume that the trajectories of robot between mapping and localization are not far away from each other to ensure the existence of similar subsurface features. The similar trajectory location assumption can be easily achieved when the robots/autonomous vehicle moves along the lane and the pre-scann mapping process is sufficiently dense.

C. Notations and Problem Definition

To describe our problem, we define the following notations.

- $\{G\}$: A 3D GPR ego-centric world coordinate system defined by the initial position of the GPR, with $Y - Z$ representing the horizontal ground plane, Y pointing to
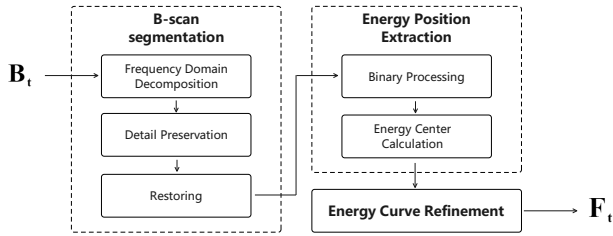
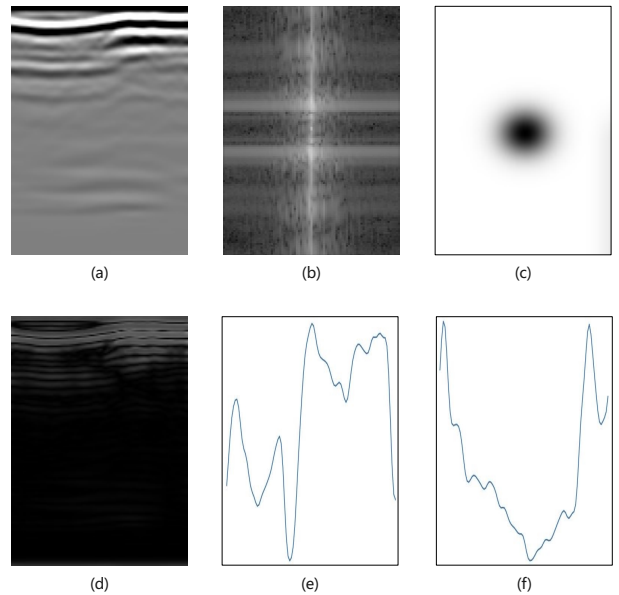Fig. 3. The feature extraction algorithm diagram.

Fig. 4. The intermediate results generated in algorithm. Grayscale is used to represent signal strength in (a)-(d). Brighter color means stronger signal. All images are using the same B-scan coordinate as $B_t(x, y)$.

the motion direction of the GPR, and X pointing to the downward direction.

- $\mathbf{P}_t \in \{G\}$, a 3D coordinate for the GPR position at time t. This is the current time at the localization step.
- W and L are the maximum width index and the maximum depth index of a B-scan image, respectively. Note that L is also the maximum depth index of the A-scans. They can be understood as the width and height of the B-scan image.
- $A = \{a_x | x = 1, 2, 3, \ldots, L\}$, A-scan signal obtained by GPR. x is the depth index of the signal value in A.
- $B_t(x, y) = \{a_x | a_x \in A_y, \text{ and } y = 1, 2, 3, \ldots, W\}$ is x-th signal values in the y-th A scans A_y at time t. Therefore, it forms an image indexed by (x, y) at time t, $1 \le x \le L$ is the depth range of each A_y, and $1 \le y \le W$ is the horizontal position index range along the GPR motion trajectory.
- $\mathbf{F}_t$, DEC feature extracted from $B_t(x, y)$ and will be explained in detail later.
- $\mathcal{M} = \{(\mathbf{F}_j, \mathbf{P}_j) | j = 1, 2, 3, \ldots, N\}$, the prior map constructed as the j-th set of DEC features $\mathbf{F}_j$ and the corresponding 3D GPR positions $\mathbf{P}_j \in \{G\}$ where $\mathbf{F}_j$ contain DEC feature just like $\mathbf{F}_t$.

With the notations above, we define our problem as follows.

Definition 1: With a subsurface feature map $\mathcal{M}$ built. Given $B_t(x, y)$, extract DEC features $\mathbf{F}_t$ from $B_t(x, y)$ and perform feature matching with $\mathcal{M}$ to find robot location $\mathbf{P}_t$.

IV. ALGORITHM

We will begin with the introduction of the new DEC feature descriptor design. After DEC features are extracted from the current B scan, they will be matched with the prior subsurface feature map to localize the robot.

A. Feature Extraction

Since a GPR does not directly provide 3D positions for the scanned objects but a set of cluttered radar reflections (B-scan images), the feature extraction from GPR data is a new challenging problem. Thus, we design a novel feature descriptor, named as the Dominant Energy Curve (DEC), to efficiently extract features from noisy GPR B-scan images. DEC describes the variation of the positions of the energy centers in a B-scan image which corresponds to the most dominant signal reflection. As shown in Fig. 3, DEC features can be extracted using the following three steps.

1) B-scan Segmentation: A B-scan image consists of a series of consecutive A-scans. From the original B-scan image (see Fig. 4(a)), it is hard to identify the dominant energy position variation due to many other noisy reflections in the background. Our goal is to suppress the noisy background reflections and focus on salient ones.

Frequency Domain Decomposition: We map a B-scan image to a two-dimensional frequency domain, which can be seen as a superposition of a series of plane waves. A single plane wave is determined by a normal vector $\overrightarrow{n}$, the length of $\overrightarrow{n}$, the amplitude and phase of the wave. Among them, low-frequency waves make up outlines and high-frequency waves make up details. The Fourier transform is adopted to achieve this process,

$$F(u, v) = \sum_{x=0}^{L-1} \sum_{y=0}^{W-1} B_t(x, y) e^{-j2\pi(\frac{ux}{L} + \frac{vy}{W})} \quad (1)$$

where $F(u, v)$ is the frequency domain graph shown in Fig. 4(b), (u, v) is the coordinate in the frequency domain graph and also the parameter to determine a plane wave.

Detail preservation: The high-frequency waves are at the edge of the frequency domain while the low-frequency waves are at the center, and those high-frequency waves form parts in which the grayscale value changes significantly. To better focus on the change in dominant energy positions of the B scan, it is necessary to remove the low-frequency fluctuations and keep the high-frequency detail information. A Gaussian high-pass filter is used,

$$H(u, v) = 1 - e^{-D(u,v)^2/2D_0^2}, \quad (2)$$

where $D(u, v)$ is the l_2 distance from point (u, v) to the center point coordinate $(\frac{W}{2}, \frac{L}{2})$, D_0 is the radius of the

Gaussian high-pass filter which is a constant. $H(u, v)$ is the Gaussian high-pass filter and shown in Fig. 4(c).

The dot product between $F(u, v)$ and $H(u, v)$ is a new two-frequency domain with the low-frequency signal removed,

$$G(u, v) = F(u, v) \cdot H(u, v). \quad (3)$$

Restoring: Recombine these high-frequency plane waves into a new B-scan image with only details, and apply the inverse Fourier transform on $G(u, v)$,

$$B_t'(x, y) = \frac{1}{WL} \sum_{u=0}^{L-1} \sum_{v=0}^{W-1} G(u, v) e^{-j2\pi(\frac{ux}{L} + \frac{vy}{W})}, \quad (4)$$

where $B_t'(x, y)$ is the new B-scan image block with only high frequency details. $B_t'(x, y)$ is shown in Fig. 4(d). Compared to Fig. 4(a), many scattered reflection signals are reduced in Fig. 4(d) and texture of energy changes are clearly shown. With the B scan segmentation step completed, we are ready to extract the energy position from $B_t'(x, y)$.

2) Energy Position Extraction: $B_t'(x, y)$ is composed of a series of new A-scan A_y' that keeps peaks and suppresses low amplitude and low frequency fluctuations,

$$A_y'(x) = B_t'(x, y), \ \forall x, y. \quad (5)$$

Binary Processing: For each filtered A-scan signal A_y', the prominent peak positions indicate significant reflections occurring when the electromagnetic wave encounters objects or interfaces where the dielectric constant varies. To enhance those prominent reflections, we perform binary processing on A_y'. The threshold t_y is,

$$t_y = \frac{\sum_{x=1}^{m} A_y'(x)}{m}, \quad (6)$$

where m is the length of the signal, $A_y'(x)$ is the value of the signal at position x.

The amplitude of an electromagnetic wave decreases when it spreads deeper into the ground and the reflections at deep layers are weak. As a result, to better extract features deep under the ground, each A-scan signal A_y' is evenly divided into shallow and deep parts and will be processed separately: the signals in the upper half are named shallow signal and those in the lower half are named deep signal.

$$A_y' = \{A_{\text{shallow}}', A_{\text{deep}}'\}. \quad (7)$$

Calculate thresholds t_y^{shallow} and t_y^{deep} for A_{shallow}' and A_{deep}' with the adaptive threshold in (6), respectively. Use these two thresholds to transform A_{shallow}' and A_{deep}' into binary signals b_y^{shallow} and b_y^{deep} with a high value of 255 if the element value of the A scan sub-sequence is above the corresponding threshold or a low value of 0 otherwise, respectively.

Energy Center Calculation: Now let us calculate energy center positions p_y^{shallow} and p_y^{deep} for shallow and deep layers, respectively, set p_y^{shallow} as an example, with

$$p_y^{\text{shallow}} = \frac{\sum_{k=1}^{q} x_k^{\text{shallow}}}{q}, \quad (8)$$

where q is the number of the positions where signal value in b_y^{shallow} is 255. x_k^{shallow} is the position where the signal value in b_y^{shallow} is 255. Similarly, the result p_y^{deep} can be obtained. When performing the above operations on all A_y' in $B_t'(x, y)$, we can obtain two curves $\mathbf{D}_t^{\text{shallow}}$ and $\mathbf{D}_t^{\text{deep}}$,

$$\mathbf{D}_t^{\text{shallow}} = \{p_y^{\text{shallow}} | i = 1, 2, 3, \ldots, W\}, \quad (9)$$
$$\mathbf{D}_t^{\text{deep}} = \{p_y^{\text{deep}} | i = 1, 2, 3, \ldots, W\}. \quad (10)$$

$\mathbf{D}_t^{\text{shallow}}$ and $\mathbf{D}_t^{\text{deep}}$ represent changes in energy positions in the shallow and deep layers of the B-scan image $B_t(x, y)$, respectively. To obtain reliable features, it is necessary to proceed with the refinement step.

3) Energy Curve Refinement: It is inevitable that there is a small amount of high-frequency noise left, which can lead to false peaks. False peaks will significantly interfere with the feature matching process. To remove these false peaks, Continuous Wavelet Transform (CWT) is used to decompose signals into a combination of wavelets with different time and scale parameters. Discrete Wavelet Transform (DWT) [18] is to discrete the parameters in CWT, use $\mathbf{D}_t^{\text{shallow}}$ as an example,

$$T(a, b) = \frac{1}{\sqrt{a}} \int_{-\infty}^{+\infty} \mathbf{D}_t^{\text{shallow}}(n) \psi(\frac{n-b}{a}) dn \quad (11)$$

where, $T(a, b)$ is the time-frequency domain, a is a scale parameter and b is the time parameter, $\psi(\frac{n-b}{a})$ is the wavelet function used in DWT.

After the transformation, recombine the low-frequency wavelets in $T(a, b)$ into a new signal that is shallow DEC and defined as $\mathbf{F}_t^{\text{shallow}}$. Similarly, apply DWT on $\mathbf{D}_t^{\text{deep}}$ to get $\mathbf{F}_t^{\text{deep}}$. Finally, the resulting $\mathbf{F}_t$ is obtained as,

$$\mathbf{F}_t = \{\mathbf{F}_t^{\text{shallow}}, \mathbf{F}_t^{\text{deep}}\}, \quad (12)$$

where $\mathbf{F}_t$ is the feature of $B_t(x, y)$. Samples of $\mathbf{F}_t^{\text{shallow}}$ and $\mathbf{F}_t^{\text{deep}}$ are shown in Figs. 4(e) and 4(f), respectively.

B. Prior Subsurface Mapping

As we mentioned before, our localization method depends on prior mapping which is the process is constructing the subsurface map $\mathcal{M}$. $\mathcal{M}$ is a combination of Euclidean 3D positions of the robot when receiving A-scans and DECs. After the robot travels along the entire mapping trajectory, it generates a long B-scan image. Slice the long B-scan image according to the width of W and get B scan image segments. Each B-scan image feature extracted from feature extraction is composed of shallow DEC and deep DEC. The whole subsurface energy position variation curve is constructed by connecting the DECs of the same layer together in chronological order. With the Euclidean 3D positions recorded when capturing, each A-scan corresponds to a Euclidean 3D position in the world frame. All 3D positions and the corresponding DECs together form $\mathcal{M}$.

C. Localization by Searching and Feature Matching

We feed the DEC features extracted from the current GPR observations into PSO for localization in the subsurface map.
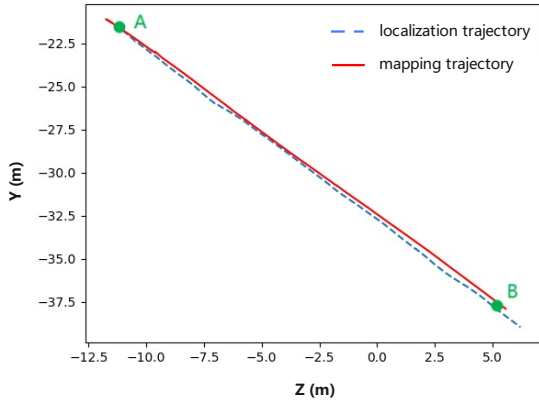
Fig. 5. Example trajectory segments from a basement showing the similar trajectory requirement between mapping and localization (*nsh_b*) environment in CMU-GPR dataset.

Denote N_p as the total number of particles, w_m as weight of the m-th particle, and $\mathbf{X}_m \in \{G\}$ as the 3D coordinate of the m-th particle in $\mathcal{M}$.

For the m-th particle, we compute the difference between the observed features $\mathbf{F}_t$ and the features $\mathbf{F}_j$ in the prior map as

$$d_m = \|\mathbf{F}_t^{shallow} - \mathbf{F}_j^{shallow}\|^2 + \|\mathbf{F}_t^{deep} - \mathbf{F}_j^{deep}\|^2 \qquad (13)$$
$$s.t. \quad \mathbf{X}_m = \mathbf{P}_j,$$

where $\| \cdot \|$ denotes the Mahalanobis distance.

Then w_m is computed by normalizing d_m to $[0, 1]$ interval by Gaussian distribution,

$$w_m = \frac{1}{\sqrt{2\pi}\sigma} e^{-\frac{d_m^2}{2\sigma^2}}, \qquad (14)$$

where σ denotes the estimated error.

With w_m obtained, we perform resampling using a multinomial resample algorithm. The weight update and resampling processes are executed iteratively. The robot location $\mathbf{P}_t$ can be obtained as

$$\mathbf{P}_t = \arg\min_{\hat{\mathbf{P}}_t} \sum_{m=1}^{N_p} d_m$$
$$s.t. \quad \hat{\mathbf{P}}_t = \frac{1}{N_p} \sum_{m=1}^{N_p} \mathbf{X}_m, \qquad (15)$$

where $\hat{\mathbf{P}}_t$ denotes the estimated value of $\mathbf{P}_t$.

V. Experiments

We evaluate our proposed GPR-based localization method on the public CMU-GPR dataset. First, we briefly introduce the data set. Then, the results of the feature similarity verification between the maps and the observations are presented to validate the effectiveness of our designed DEC features. After that, we evaluate our method qualitatively and quantitatively by comparing our method with several counterparts. Finally, we discuss the computational speed of our method to show its potential for real-time applications.
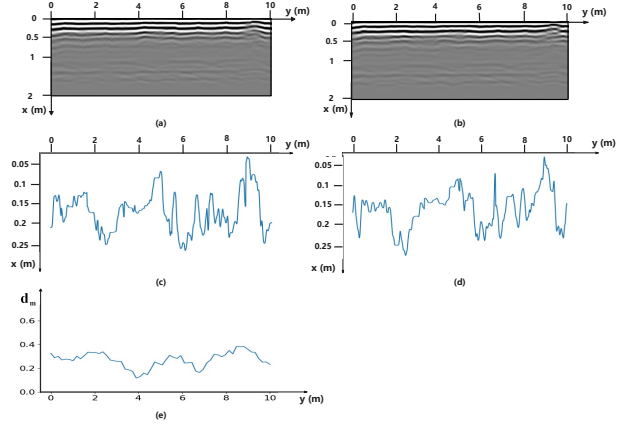

Fig. 6. Illustrations of B-scan segment from the prior map (a) and current observation (b) at a parking garage (*gates_g*) environment, and $\mathbf{F}_j^{\text{shallow}}$ (c), $\mathbf{F}_t^{\text{shallow}}$ (d), difference value d_m (e) between $\mathbf{F}_j$ and $\mathbf{F}_t$ when $\mathbf{P}_j$ in (a) is the closest to $\mathbf{P}_t$ in (b).
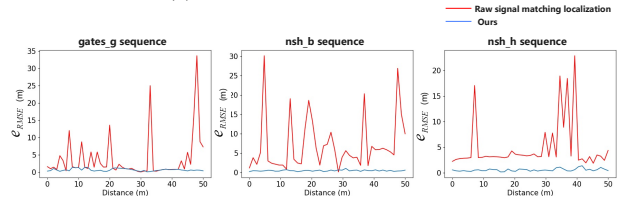

Fig. 7. e_{RMSE} over time in three environments.

A. Dataset Introduction

Our experiments are performed on CMU-GPR dataset [15] which is an open-source GPR dataset specially for research in subsurface-aided robot navigation. This dataset contains several distinct trajectory sequences in three GPS denied scenarios, including 7 trajectories in a basement (*nsh_b*), 5 trajectories in a factory floor (*nsh_h*) and 3 trajectories in a parking garage (*gates_g*). For the three environments, the total trajectory length of *gates_g*, *nsh_b nsh_h* data sets are 365m, 264m, and 90m, respectively. Measurements collected on each trajectory include a single-channel GPR, a camera, a wheel encoder, and total station readings.

Fig. 5 illustrates an example of a segment of a robot trajectory sequence. From Fig. 5, these two trajectories travel from B to A but do not overlap completely. In our experiments, we select one trajectory from the sequence as the referred map. Data from the total station provide an accurate position for each position on the map. We choose a different trajectory for robot localization purpose. Our task is to perform robot localization while traveling along the trajectory segment from the start point to the end point. Note that the two trajectories are adjacent but not overlapping.

B. Feature Similarity Verification

Since the proposed DEC feature is the foundation for the matching and localization of the following features, we verify it first. Figs. 6 (a) and (b) show examples of the original B scan segments for the map trajectory and the localization trajectory, respectively. The extracted $\mathbf{F}_j^{\text{shallow}}$ and $\mathbf{F}_t^{\text{shallow}}$ by our algorithm are shown in Figs. 6(c) and (d), respectively. Their
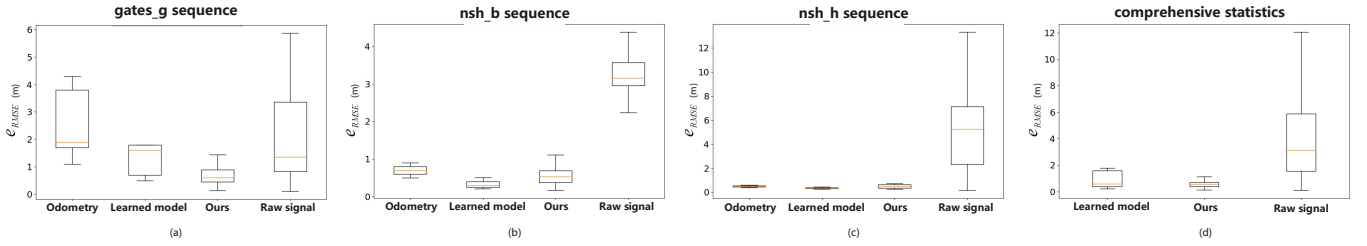
Fig. 8. (a), (b) and (c) are the maximum value, upper quartile, median, lower quartile, and minimum value about e_{RMSE} for each testing environment, (d) is the comprehensive statistics about the three environments.

difference value d_m, is shown in Fig. 6(e). DEC differences reflect the differences between the robot's real positions and the corresponding positions on the map. The low value in the DEC difference implies the high similarity between the features extracted when the robot moves along the adjacent but non-overlapping trajectories.

C. Field Test for GPR-based Localization

The three existing methods to which we compare our algorithm are:

- Odometry. The method is to localize the robot using wheel-encoder measurements by dead-reckoning.
- Raw signal matching. The method employs Pearson correlation coefficient to calculate the similarity between the raw GPR signals. The similarity values between a series of A-scan signals actually observed and the signals on the map are then fed into the particle filter to perform the localization. Pearson correlation between two independent GPR A scan signals A_i and A_j is $r(A_i, A_j) = \frac{\sum_{x=1}^{n}(A_i(x)-\overline{A}_i)(A_j(x)-\overline{A}_j)}{\sqrt{\sum_{x=1}^{n}\left(A_i(x)-\overline{A}_i\right)^2}\sqrt{\sum_{x=1}^{n}\left(A_j(x)-\overline{A}_j\right)^2}}$, where n is the length of the signals.
- The learned model [14], which is a machine learning-based GPR localization method that performs inference on a factor graph.

To quantitatively assess the performance of different localization methods, root mean squared error (RMSE) e_{RMSE} is used,

$$e_{\mathrm{RMSE}} := \sqrt{\frac{\sum_{i=1}^{N}\|P_i, P_{\mathrm{totalStation}}\|_2^2}{N}}, \qquad (16)$$

where $\|\cdot\|_2$ is l_2 norm, N denotes the number of measurements at current position, $P_{\mathrm{totalStation}}$ denotes the position measured by the total station, and P_i is the position obtained from the i-th estimation.

Fig. 7 shows e_{RMSE} of the raw signal matching algorithm and our proposed algorithm in three environments, where we can see that the e_{RMSE} curve of the raw signal matching algorithm has some extremely high peaks caused by the mismatch in the A-scan signals. As a result, the PSO algorithm cannot converge correctly. On the other hand, we can find that our proposed algorithm recovers the robot's locations stably and close to the ground truth.

Fig. 8 shows the e_{RMSE} statistics of the four algorithms compared in three testing environments and the overall performance. The odometry method has the largest error especially

in *gates_g* since there are more turns in the parking garage scenario. The raw signal matching algorithm often traps in false localization caused by feature mismatching. Since the Odometry and the Raw signal methods perform much worse than ours and the learned model, we only focus on the comparison with the learned model. Our algorithm outperforms the learned model in parking garage and achieves similar performance in factory floor, but is slightly inferior in basement. Note that loop closure is performed in the learned model algorithm. Since our method does not include loop closure, it is more applicable in the general scenario, and its performance can be easily improved further if it is combined with those techniques. Quantitatively, the mean localization errors of our proposed algorithm are 0.47m, 0.52m, and 0.57m in the three scenarios, respectively. Fig. 8(d) shows the comprehensive statistics of the three environments, this is done by interpolating and aggregating the results based on trajectory length. The mean value e_{RMSE} of our algorithm is 0.50m while the learned model is 0.59m according to [14] and the total distance weight of each environment. We do not include odometry results in the combined statistics because its error drift is linear to the trajectory length.

VI. CONCLUSION AND FUTURE WORK

We reported a novel robot localization method by observing subsurface characteristics using a single-channel GPR onboard. An efficient feature descriptor, DEC, was specifically designed for the interpretation of GPR data. The metric subsurface map was built by extracting DEC features along the robot's trajectories with known positions. As a result, our method was able to localize the robot using feature matching. Our proposed method was tested on the public CMU-GPR dataset, achieving satisfactory localization performance compared to the existing state-of-the-art.

In the future, we will implement our method in a distributed and parallel manner to achieve real-time localization performance. A new spatial data structure will be developed and incorporated to increase the speed of map matching. A more sensory fusion approach will be developed to increase robustness and reduce computational needs.

REFERENCES

[1] R. S. Lim, H. M. La, and W. Sheng, "A robotic crack inspection and mapping system for bridge deck maintenance," *IEEE Transactions on Automation Science and Engineering*, vol. 11, no. 2, pp. 367–378, 2014.

[2] H. Ahmed, H. M. La, and N. Gucunski, "Review of non-destructive civil infrastructure evaluation for bridges: State-of-the-art robotic platforms, sensors and algorithms," *Sensors*, vol. 20, no. 14, p. 3954, 2020.

[3] H. Chen and A. G, "Buried utility pipeline mapping based on multiple spatial data sources: a bayesian data fusion approach," in *IJCAI*, vol. 11. IEEE, 2011, pp. 2411–2417.

[4] F. Yang, X. Qiao, Y. Zhang, and X. Xu, "Prediction method of underground pipeline based on hyperbolic asymptote of gpr image," in *Ground Penetrating Radar (GPR), 2014 15th International Conference on*. IEEE, 2014, pp. 674–678.

[5] H. Li, N. Li, R. Wu, H. Wang, Z. Gui, and D. Song, "Gpr-rcnn: An algorithm of subsurface defect detection for airport runway based on gpr," *IEEE Robotics and Automation Letters*, vol. 6, no. 2, pp. 3001–3008, 2021.

[6] N. Li, R. Wu, H. Li, H. Wang, Z. Gui, and D. Song, "M2fnet: Multi-modal fusion network for airport runway subsurface defect detection using gpr data," *IEEE Transactions on Geoscience and Remote Sensing*, p. Early Access, 2023.

[7] P. Furgale, T. D. Barfoot, and N. Ghafoor, "Rover-based surface and subsurface modeling for planetary exploration," *Field and Service Robotics*, pp. 499–508, 2010.

[8] J. Lai, Y. Xu, R. Bugiolacchi, X. Meng, and L. Xu, "First look by the yutu-2 rover at the deep subsurface structure at the lunar farside," *Nature Communications*, vol. 11, no. 1, pp. 1–9, 2020.

[9] G. Kouros, I. Kotavelis, E. Skartados, D. Giakoumis, and G. Manacorda, "3d underground mapping with a mobile robot and a gpr antenna," in *2018 IEEE/RSJ International Conference on Intelligent Robots and Systems (IROS)*. IEEE, 2018.

[10] C. Chou, A. Kingery, D. Wang, H. Li, and D. Song, "Encoder-camera-ground penetrating radar tri-sensor mapping for surface and subsurface transportation infrastructure inspection," in *Robotics and Automation, 2018. ICRA'18. IEEE International Conference on*. Brisbane, Australia: IEEE, May 2018.

[11] C. Chou, H. Li, and D. Song, "Encoder-camera-ground penetrating radar sensor fusion: Bimodal calibration and subsurface mapping," *IEEE Transactions on Robotics*, vol. 37, no. 1, pp. 67–81, 2021.

[12] M. Cornick, J. Koechling, B. Stanley, and B. Zhang, "Localizing ground penetrating radar: A step toward robust autonomous ground vehicle localization," *Journal of field robotics*, vol. 33, no. 1, pp. 82–102, 2016.

[13] T. Ort, I. Gilitschenski, and D. Rus, "Autonomous navigation in inclement weather based on a localizing ground penetrating radar," in *International Conference on Robotics and Automation*, 2020.

[14] A. Baikovitz, P. Sodhi, M. Dille, and M. Kaess, "Ground encoding: Learned factor graph-based models for localizing ground penetrating radar," in *2021 IEEE/RSJ International Conference on Intelligent Robots and Systems (IROS)*. IEEE, 2021, pp. 5476–5483.

[15] A. Baikovit, P. Sodhi, M. Dille, and M. Kaess, "Cmu-gpr dataset: Ground penetrating radar dataset for robot localization and mapping," *arXiv*, 2021.

[16] E. Skartados, A. Kargakos, E. Tsiogas, I. Kostavelis, D. Giakoumis, and D. Tzovaras, "Gpr antenna localization based on a-scans," in *2019 27th European Signal Processing Conference (EUSIPCO)*, 2019, pp. 1–5.

[17] H. Li, C. Chou, L. Fan, B. Li, D. Wang, and D. Song, "Toward automatic subsurface pipeline mapping by fusing a ground-penetrating radar and a camera," *IEEE Transactions on Automation Science and Engineering*, vol. 17, no. 2, pp. 722–734, 2020.

[18] D. Sundararajan, *Discrete Wavelet Transform: A Signal Processing Approach*, ser. CourseSmart Series. Wiley, 2016. [Online]. Available: https://books.google.com.sg/books?id=mGhcCwAAQBAJ